Physics and Chemistry of Minerals (2020) 47:41
https://doi.org/10.1007/s00269-020-01111-9

ORIGINAL PAPER

Pressure-induced structural transition and metallization in $MnSe_2$

Baoyun Wang[1,2] · Xiaoning Wang[1,2] · Simeng Wang[1,2] · Dayong Tan[3] · Wansheng Xiao[3] · Wen Liang[4] · Maoshuang Song[1]

Received: 10 June 2020 / Accepted: 8 September 2020

Abstract
The high-pressure behavior of manganese diselenide $MnSe_2$ was investigated by synchrotron angle-dispersive X-ray diffraction (ADXRD) and infrared reflection spectroscopy equipped with a diamond-anvil cell. It was found that $MnSe_2$ with a pyrite-type structure undergoes a transformation into a disordered intermediate phase at ~ 12.5 GPa, with a ground state composed of an arsenopyrite-type structure, as confirmed by laser-heating treatment. The pyrite to arsenopyrite phase transition was found to be coupled to a large collapse in the unit-cell volume ($\Delta V \sim 19\%$) and an electronic transition from a high-spin to low-spin state for manganese cations (Mn^{2+}). With a fixed value for the pressure derivation of the bulk modulus $K' = 4$, fitting of the pressure–volume data to a second-order Birch–Murnaghan equation of state yielded isothermal bulk modulus values of $K_0 = 56.1(9)$ GPa and $K_0 = 93.1(4)$ GPa for the pyrite-type and arsenopyrite-type phases, respectively. The measured infrared reflectivity (R_{sd}) for $MnSe_2$ showed a drastic increase at pressures between 13 and 20 GPa, but became insensitive to pressure under further compression, implying a pressure-induced transition from an insulator to metallic state.

Keywords Manganese diselenide ($MnSe_2$) · Arsenopyrite-type structure · Disordered intermediate · Large volume collapse · Pressure-induced metallization

Introduction

The transition-metal di-chalcogenides TX_2 (T=Mn, Fe, Co, Ni, Cu, Zn, X=S, Se, Te) with a pyrite-type structure (spacegroup *Pa* 3, Fig. 1a) exhibit diverse electrical, magnetic and optical properties (Bither et al. 1968; Lauer et al. 1984; Ogawa 1979; Temmerman et al. 1993), and, hence, have important technical applications in many fields such as electrocatalysts for the hydrogen evolution reaction (Faber et al. 2014; Wu et al. 2019), supercapacitors and lithium-ion batteries (Gudelli et al. 2013; Yu et al. 2016), and thermoelectric materials and spin electronics (Feng et al. 2018; Houari and Blöchl 2018). Quite a large number of experimental and theoretical studies have been conducted for pyrite-type TX_2 compounds and many intriguing phenomena, such as half-metallicity, Mott–Hubbard insulator, superconducting and pressure-induced metallization, have been unveiled (Chandra et al. 2014; Honig and Spałek 1998; Houari and Blöchl 2018; Huang et al. 2018; Kakihana et al. 2018; Perucchi et al. 2009; Sidorov et al. 2011; Ueda et al. 2002; Yonggang and Ross 2010). Most pyrite-type TX_2 compounds, such as FeS_2, CoS_2 and NiS_2, can occur as natural minerals with ubiquitous distribution in the Earth's surface and deep interior, forming as a result of hydrothermal activity, magma crystallization differentiation and so on (Reich et al. 2013; Tossell et al. 1981). Especially, some of these minerals might be important components in the Earth's core, and may even exist in other planetary bodies as transition-metal sulfides are common minerals in meteorites. Therefore, the high-pressure behavior of pyrite-type TX_2 compounds may play an important role in understanding the composition and differentiation of the Earth's interior as well as that for other planets (Cohen et al. 1997).

✉ Maoshuang Song
msong@gig.ac.cn

1 State Key Laboratory of Isotope Geochemistry, Guangzhou Institute of Geochemistry, Chinese Academy of Sciences, Guangzhou 510640, China

2 College of Earth and Planetary Sciences, University of Chinese Academy of Sciences, Beijing 100049, China

3 Key Laboratory of Mineralogy and Metallogeny, Guangzhou Institute of Geochemistry, Chinese Academy of Sciences, Guangzhou 510640, China

4 Key Laboratory of High Temperature and High Pressure Study of the Earth's Interior, Institute of Geochemistry, Chinese Academy of Sciences, Guiyang 550081, China

Published online: 25 September 2020

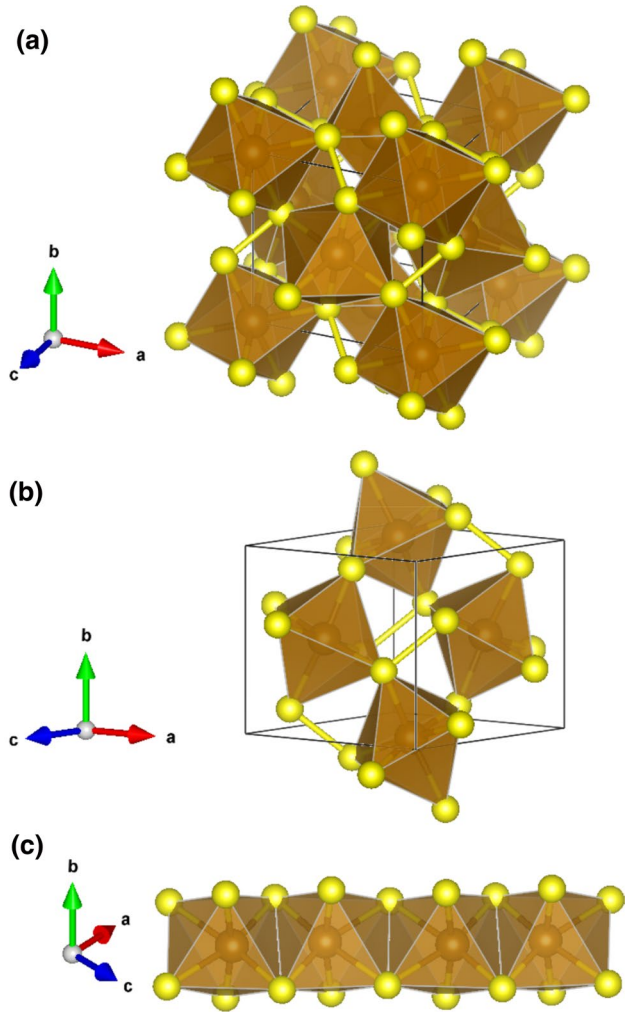

Fig. 1 Typical crystal structures of TX_2 transition-metal di-chalcogenides: **a** the pyrite-type phase, **b** the arsenopyrite-type phase, **c** an edge-sharing chain of TX_6 octahedra in [101] direction of arsenopyrite-type phase. The large brown spheres are T (transition-metal) atoms and the small yellow spheres are X (chalcogenide) atoms

Normally, the 3d electrons of the transitional metal T^{2+} cations present in TX_2 compounds with a pyrite-type structure are arranged in the low-spin electronic configuration. Such low-spin TX_2 compounds can maintain their pyrite-type structure over a wide *P–T* stability field and the unit-cell parameters for such compounds follow Vegard's law or the rigid sphere model, varying linearly with the size of the transitional-metal cations from Fe to Zn (Bither et al. 1968; Lauer et al. 1984; Ogawa 1979; Temmerman et al. 1993). Unlike other TX_2 compounds, the manganese di-chalcogenides MnX_2 (X=S, Se and Te) are abnormal in that the 3d electrons of the Mn^{2+} cations are in a high-spin electronic state ($t_{2g}^3 e_g^2, S = \frac{5}{2}$), and they possess larger unit-cell parameters than low-spin TX_2 compounds (Feng et al. 2018). For instance, the lattice parameter *a* for MnS_2 has been reported to be 6.1013 Å, which is much larger than that for ZnS_2 (5.9542 Å) and FeS_2 (5.4190 Å) (Bither et al. 1968; Feng et al. 2018).

A few experimental studies have been conducted to investigate the structural behavior as well as magnetic and electrical properties of MnT_2 compounds under high-pressure and/or low-temperature conditions. MnS_2, which is paramagnetic at ambient conditions, undergoes a first-order phase transition to an antiferromagnetic state with very small volume change when cooled below the Neel temperature $T_N = 48.2$ K at ambient pressure, and the transition temperature T_N increases with pressure at a rate of $dT_N/dP = 4.83$ K/GPa (Hastings et al. 1959; Sidorov et al. 2018). A paramagnetic–antiferromagnetic transition has also been observed in $MnSe_2$ and $MnTe_2$ (Chattopadhyay et al. 1987; Vulliet et al. 2001). Under compression, MnS_2 transforms from a high-spin (HS) to low-spin (LS) electronic state at around 12 GPa, accompanied by a giant volume collapse (Bargeron et al. 1971; Chattopadhyay and Schnering 1985; Chattopadhyay et al. 1986). The low-spin phase of MnS_2 was determined as a marcasite-type structure (spacegroup P*nnm*) using conventional laboratory energy-dispersive X-ray diffraction (Chattopadhyay and Schnering 1985). However, while synchrotron radiation energy-dispersive X-ray diffraction was applied, the low-spin phase of MnS_2 appeared as an unidentified disordered phase even though it was assumed to have a marcasite-type structure. Likewise, $MnTe_2$ was observed to transit to the low-spin electronic state with an abrupt volume decrease of 16% at around 8 GPa, and the low-spin $MnTe_2$ phase was found to possess a marcasite-type structure under non-hydrostatic conditions using conventional XRD or a pyrite-type structure under quasi-hydrostatic conditions (Fjellvåg et al. 1995, 1985). It is particularly interesting that the HS–LS transition for $MnTe_2$ is accompanied by a pressure-induced metallization leading to a non-magnetic Mn^{2+} ground state (Vulliet et al. 2001). Recent synchrotron radiation XRD experiments combined with theoretical calculations revealed that MnS_2 transits into a disordered intermediate at ~ 11.8 GPa with a ground state that has a arsenopyrite-type structure (spacegroup $P2_1/c$, Fig. 1b, c), and accompanied by a HS–LS transition and a giant volume collapse of ~ 22%. However, the predicted metallization was not found to occur in the arsenopyrite-type phase of MnS_2 because metallic Mn–Mn dimers are separated by a long Mn–Mn bondlength (Durkee et al. 2019; Kimber et al. 2014; Fig. 1c). Even though MnS_2 is predicted to transit into a low-spin state under compression without metallization, which is different from $MnTe_2$, there is no experimental evidence for its transport property to support this prospect.

$MnSe_2$ displays interesting electronic and antiferromagnetic properties, which is of potential applications in many technical fields such anode material for sodium-ion and lithium-ion batteries as well as spintronics (Kan et al.

2014; Pathak et al. 2020). However, in contrast to MnS_2 and $MnTe_2$, no experiment for the high-pressure behavior of $MnSe_2$ has ever been performed until now. To obtain a thorough understanding of the high-pressure behavior of MnX_2 compounds, including the HS–LS transition, the pressure-induced metallization and the effect of element substitution from S to Te, experimental works for $MnSe_2$ at high pressure are necessary. In this study, we carried out in situ synchrotron XRD and infrared reflection spectroscopy measurements for $MnSe_2$ at high pressures and ambient temperature so as to investigate its structural behavior and pressure-induced metallization.

Experimental details

The $MnSe_2$ sample with a pyrite-type structure used in this study was synthesized by following the hydrothermal method reported by Wang et al. (2006). All the chemicals including manganese sulfate monohydrate ($MnSO_4{\cdot}H_2O$), sodium hypophosphite ($NaH_2PO_2{\cdot}H_2O$) and Se powders of analytical pure grade were purchased from Alfa-Aesar. At first, stoichiometric amounts of $MnSO_4{\cdot}H_2O$ and Se (1:2 in mole ratio) were dissolved into 50-ml distilled water, and an appropriate amount (0.01 mol) of $NaH_2PO_2{\cdot}H_2O$ was added into the solution. Then, the mixed solution was transferred into and sealed inside a Teflon-lined autoclave with a capacity of 100 ml. The sealed autoclave was heated at 150 °C for 12 h in an electrical oven, and, then, naturally cooled down to room temperature. Finally, a black solid product was collected by filtrating the heated solution, which was washed with distilled water and ethanol and dried at 60 °C in a vacuum oven to get rid of impurities. The synthesized product was composed of small cube-like crystals approximately 80 μm in size that were composed of pure $MnSe_2$ with a pyrite-type structure as confirmed by Raman spectroscopy and X-ray diffraction.

High-pressure angle-dispersive X-ray diffraction (ADXRD) experiments were performed for $MnSe_2$ at beamline 4W2 of the Beijing Synchrotron Radiation Facility (BSRF) and beamline 15U1 of the Shanghai Synchrotron Radiation Facility (SSRF). An incident monochromatic X-ray beam with a wavelength of 0.6199 Å was focused onto a ~ 5 μm × 5 μm spot on a sample for experiments at the SSRF beamline 15U1, and onto a ~ 20 μm × 10 μm spot on a sample for experiments at the BSRF beamline 4W2. X-ray diffraction patterns for samples were recorded by a Mar345 image plate. The distance between sample and the image plate was calibrated using CeO_2 as a standard. High pressure was generated by a short symmetric diamond-anvil cell (DAC) with a culet size of 400 μm. The synthesized $MnSe_2$ crystals were crushed into powders and pressed into a pellet with a thickness of approximately 15 μm using a DAC with no gasket, and a piece of the pellet approximately 60 μm in diameter was prepared and chosen as a sample. This $MnSe_2$ sample, together with several ruby chips, was loaded inside a 190-μm-diameter hole made at the center of a pre-indented area of a stainless gasket. Pressure was determined by the standard method of ruby fluorescence spectroscopy (Mao et al. 1986). Two series of ADXRD experiments were conducted, one with argon as the pressure transmitting medium (PTM) and the other without a PTM, and the ADXRD data were collected during both the compression and decompression processes. For experiments with a PTM, the sample was heated after reaching the maximum pressure of 22.5 GPa using an SPI fiber laser (1064 nm). The collected ADXRD data were analyzed by integrating two-dimensional images as a function of 2θ using the Dioptas program to obtain conventional one-dimensional diffraction patterns (Prescher and Prakapenka 2015). Structural refinements and lattice parameters were analyzed by the GSAS–EXPGUI (Toby 2001).

High-pressure infrared (IR) reflection spectra up to 28.3 GPa were measured over a wavenumber range of 600–7500 cm^{-1} using a Bruker Vertex 70 FTIR spectrometer combined with a Hyperion-2000 IR microscope equipped with a HgCdTe (MCT) detector. Pressure was generated by a short symmetric diamond-anvil cell with type IIa diamond anvils with a 400-μm culet. The powdered $MnSe_2$ sample was loaded inside the sample chamber and compressed directly by diamond anvils without using a pressure transmitting medium. Several ruby chips were placed into the sample chamber to determine the pressure. The optical geometries used for the IR reflectivity measurements are shown in Fig. 2. The reflectivity of the sample–diamond interface, denoted as $R_{sd}(\omega)$, can be calculated using the following formula:

$$R_{sd}(\omega) = \left[\frac{I_{sd}(\omega)}{I_d(\omega)} \Big/ \frac{I_e(\omega)}{I_{d'}(\omega)}\right] R_{dia},$$

where I_{sd} and I_d are the intensities reflected, respectively, from the sample–diamond culet interface and the external diamond–air interface at each pressure point, and I_e and $I_{d'}$ are the intensities reflected, respectively, from the air–diamond culet interface and the external diamond–air interface for the empty cell. R_{dia} is the reflectivity of diamond in air, which can be fixed to 0.167 (Rabia et al. 2014).

Results and discussions

The structural evolution of $MnSe_2$ under compression was investigated by synchrotron angle-dispersive X-ray diffraction equipped with a diamond-anvil cell. At first, a series of experiments were conducted under quasi-hydrostatic pressures up to 22.5 GPa using argon as a pressure transmitting

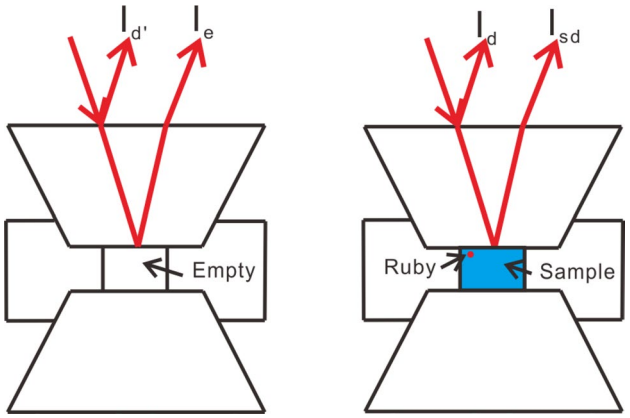

Fig. 2 The optical geometries used for infrared reflectivity measurements in a diamond-anvil cell

medium, the collected X-ray diffraction (XRD) data are presented in Fig. 3. Figure 3a shows the XRD patterns collected during the compression process. The diffraction pattern measured at 2.4 GPa can be indexed well to a pyrite-type structure. $MnSe_2$ was found to maintain the pyrite-type structure up to 12.1 GPa as no significant change was observed except for a slight diffraction peak shift and broadening. Several new diffraction peaks, as marked by pound signs, were observed in the diffraction pattern at 12.8 GPa. Such discontinuous changes indicate a transition for $MnSe_2$ into a new high-pressure phase. The phase transition was completed below 16.5 GPa, as all diffraction lines for the low-pressure pyrite-type phase of $MnSe_2$ were observed to disappear in the diffraction pattern at 16.5 GPa. At pressures of 16.5 GPa and above, the XRD patterns are nearly identical, implying that $MnSe_2$ preserves the same crystal structure. However, the diffraction peaks due to the new high-pressure phase are very broad, rendering structural refinements impossible.

To improve the quality of the diffraction pattern for the new high-pressure phase, we heated the $MnSe_2$ sample to approximately 1500 K at 22.5 GPa using an SPI fiber laser (1064 nm), followed by quenching to ambient temperature. The pressure of the sample was found to decrease to 21.2 GPa after laser heating. Figure 3b shows the XRD patterns collected for the laser-heated $MnSe_2$ sample during the decompression process. It can be seen that after laser heating treatment, the broad diffraction peaks due to the new high-pressure phase in the 22.5 GPa pattern evolve into sharp peaks in the 21.2 GPa pattern, and more peaks can be distinguished. Upon decompression, $MnSe_2$ continued to show almost an identical diffraction pattern at pressures down to 6.6 GPa, and began to transit

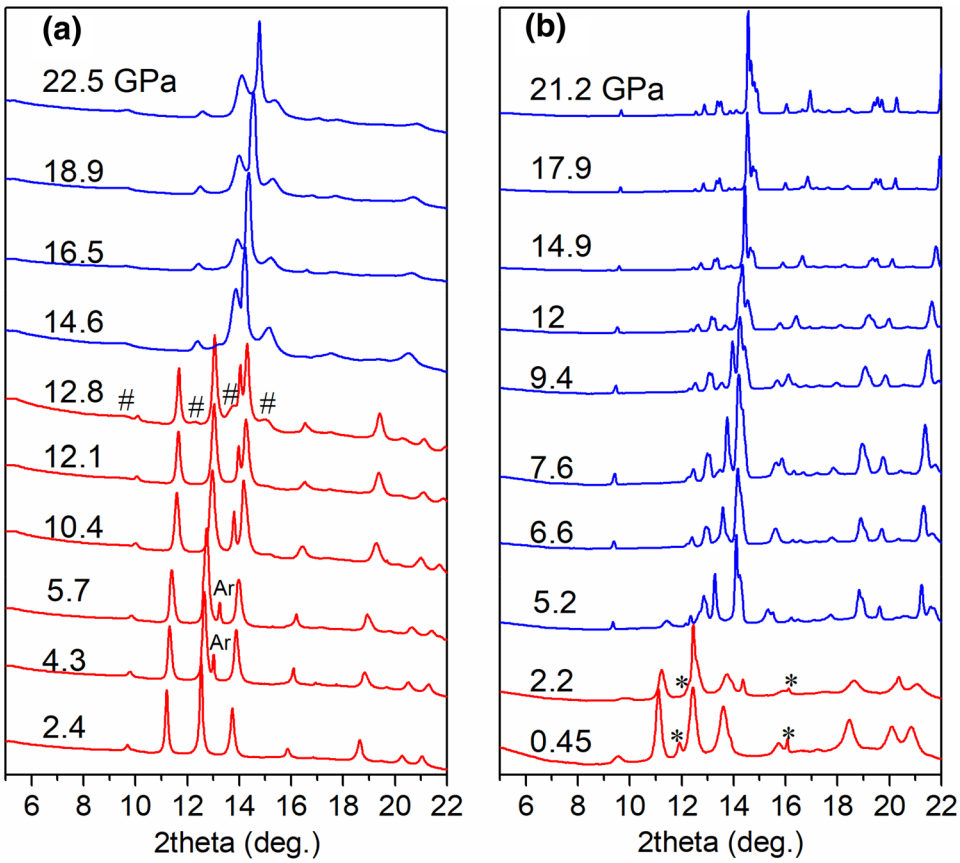

Fig. 3 Selected X-ray diffraction patterns for $MnSe_2$ obtained from experiments under quasi-hydrostatic conditions using argon as a pressure transition medium: **a** compression, **b** decompression. At 12.8 GPa, the appearance of several new peaks (marked by a pound signs (#)) implies that $MnSe_2$ begins to transit from a pyrite-type structure into a disordered intermediate phase. The decompression process was started after laser-heating the sample at the maximum pressure of 22.5 GPa. The asterisks (*) denote the diffraction peaks for a minor unknown impurity

into a pyrite-type structure at 5.2 GPa. The XRD pattern obtained at 0.45 GPa is identical to that of pyrite-type $MnSe_2$, although there exist some unknown peaks as marked by asterisks. The phase transition for $MnSe_2$ from the pyrite-type structure to the new high-pressure phase is reversible.

Figure 4 shows the results obtained from Lebail structural refinements for the XRD patterns for $MnSe_2$ at 2.4 GPa and 21.2 GPa. All the diffraction lines for the 2.4 GPa pattern can be perfectly indexed into a pyrite-type structure (spacegroup *Pa* 3) with lattice parameter $a = 6.3478$ Å and residual $\chi^2 = 0.14$ (Fig. 4a). For the 21.2 GPa pattern, most of the diffraction lines can be well indexed to the monoclinic arsenopyrite-type structure (spacegoup $P2_1/c$) with lattice parameters $a = 5.7517$ Å, $b = 5.6772$ Å, $c = 5.8025$ Å and $\beta = 113.49$ (Fig. 4b), and the Lebail refinement yields a good residual value of $\chi^2 = 0.34$. Several unknown weak peaks are observed (as marked by asterisks), which might arise from the coexistence of a minor impurity with the arsenopyrite-type phase.

The lattice parameters and unit-cell volume of the $MnSe_2$ pyrite-type and arsenopyrite phases were extracted from LeBail structural refinements for the XRD data collected during both compression and decompression processes. The pressure evolutions for the lattice parameters are plotted in Fig. 5. The relationship of lattice parameters versus pressure for both phases can be fitted by a second-order polynomial function as follows:

$$\text{Pyrite-type phase}: \quad a = 6.432(7) - 3.8(8) \times 10^{-2} P + 9.6(9) \times 10^{-4} P^2$$

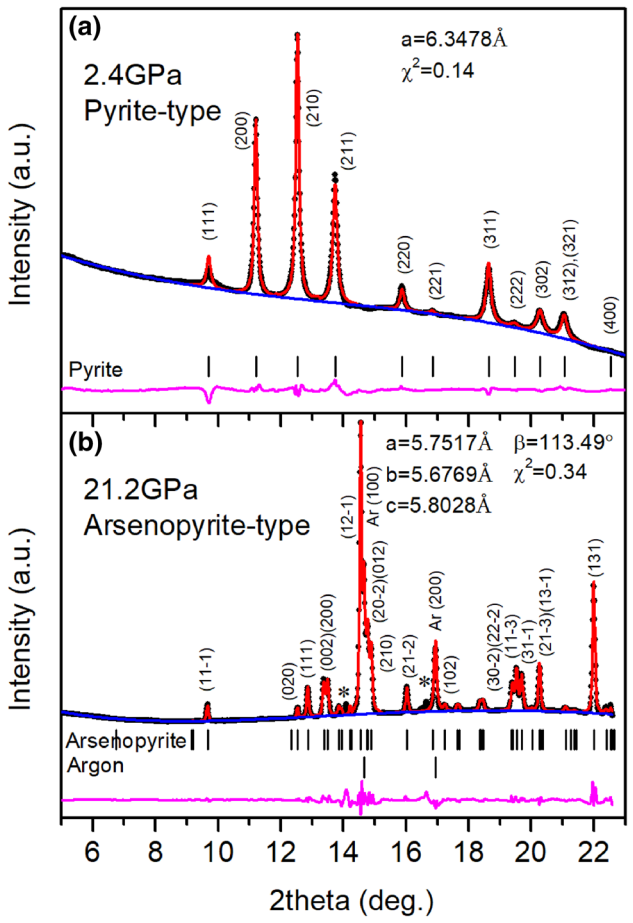

Fig. 4 LeBail refinements for different phases of $MnSe_2$: **a** pyrite-type phase at 2.4 GPa, **b** arsenopyrite-type phase at 21.2 GPa after laser-heating treatment. Experimental XRD patterns are represented by black dots; red, blue and magenta solid lines represent the refined XRD patterns, backgrounds and residuals, respectively; black vertical ticks indicate the calculated positions for the Bragg reflections for pyrite-type and arsenopyrite-type phases and argon (Ar). Diffraction peaks marked by asterisks (*) denote a minor unknown impurity coexisting with the arsenopyrite-type phase

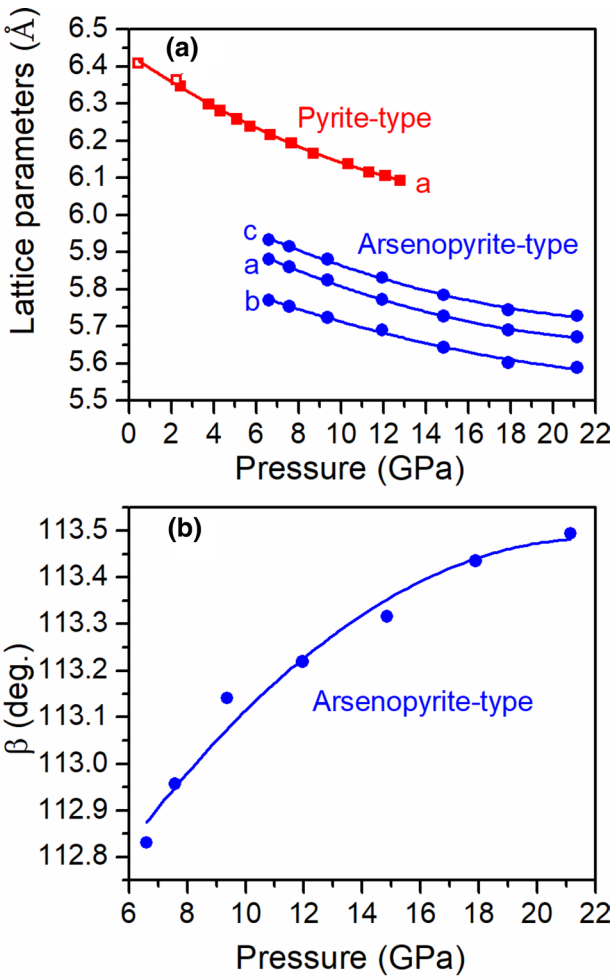

Fig. 5 **a** Pressure dependence of the lattice parameters for the pyrite-type and arsenopyrite-type phases for $MnSe_2$. **b** Pressure dependence of the monoclinic angle in the arsenopyrite-type phase. Solid squares denote the compression data, while open squares and solid circles denote decompression data

Arsenopyrite-type phase:

$$a = 6.111(4) - 2.9(6) \times 10^{-2}P + 5.9(2) \times 10^{-4}P^2,$$
$$b = 5.969(9) - 2.1(6) \times 10^{-2}P + 3.6(5) \times 10^{-4}P^2,$$
$$c = 6.153(9) - 2.8(4) \times 10^{-2}P + 5.5(0) \times 10^{-4}P^2,$$
$$\beta = 112.2(4) + 0.113(3)P - 2.58 \times 10^{-3}P^2.$$

It can be seen that the pyrite-type phase is much more compressive than the arsenopyrite-type phase. The compressibility of the arsenopyrite-type phase is nearly isotropic, but its *b* axis is more incompressible. Similar anisotropic compressibility was also reported for FeAsS arsenopyrite (Fan et al. 2011). To understand further the axial compression for the pyrite-type and arsenopyrite-type phases, the individual lattice parameters were analyzed by a modified form of the Birch–Murnaghan equation of state (Nishio-Hamane and Yagi 2009), expressed as follows:

$$P = \frac{3}{2}K_{l0}\left[\left(\frac{l_0}{l}\right)^7 - \left(\frac{l_0}{l}\right)^5\right]\left\{1 + \frac{3}{4}(K_{l0}' - 4)\left[\left(\frac{l_0}{l}\right)^2 - 1\right]\right\},$$

where l_0, K_{l0} and K_{l0}' are the zero-pressure length (lattice parameter), incompressibility and the pressure derivation of incompressibility, respectively. A least-square fit of the lattice parameter data yields $K_{a0} = 57.0(14)$ GPa and $l_{a0} = 6.425(4)$ with a fixed $K_{l0}' = 4$ ($l = a$, b or c) for the pyrite-type phase, and $K_{a0} = 93.7(86)$ GPa, $K_{b0} = 110.7(84)$ GPa and $K_{c0} = 95.6(85)$ GPa, and $l_{a0} = 6.057(17)$, $l_{b0} = 5.943(12)$ and $l_{c0} = 6.106(17)$ with fixed $K_{l0}' = 4$ for the arsenopyrite-type phase. Clearly, K_{b0} of the arsenopyrite-type phase is larger than K_{a0} and K_{c0}, implying that the *b* axis is the most incompressible axis. The large impressibility of *b* axis for the arsenopyrite-type phase is speculated to relate probably to the orientation and bond-strength of Se–Se dumbbells, and the distortion of $MnSe_6$ octahedrons on the *ac* plane, which results in the larger values of lattice parameters *a* and *c* than that of lattice parameter *b*.

Figure 6 displays the pressure dependence of the unit-cell volume for pyrite-type and arsenopyrite-type phases. There exists a large volume difference between the pyrite-type and arsenopyrite-type phases. The volume change across the pyrite-arsenopyrite phase transition at 12.5 GPa was estimated to be 19%. We fitted the pressure–volume data using the second-order Birch–Murnaghan equation of state. This fitting yields a ambient-pressure bulk modulus of $K_0 = 56.1(9)$ GPa and a zero-pressure unit-cell volume of $V_0 = 265.4(3)$ Å^3 for the pyrite-type phase, and values of $K_0 = 93.1(4)$ GPa and $V_0 = 203.1(7)$ Å^3 for the arsenopyrite-type phase with the pressure derivative of the bulk modulus K' fixed to 4. The arsenopyrite-type phase for $MnSe_2$ exhibits a much larger incompressibility than the pyrite-type phase.

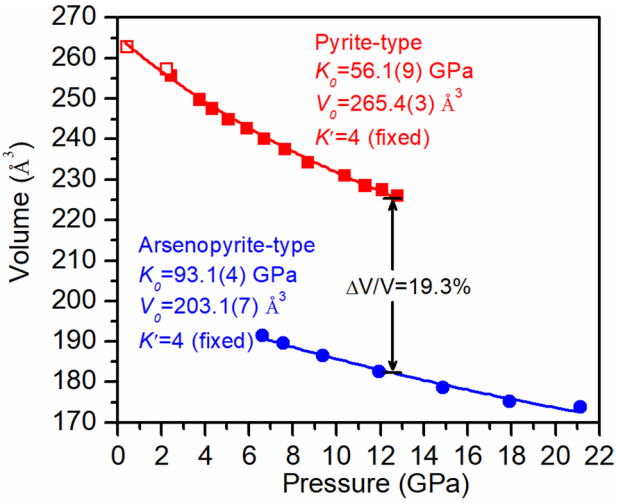

Fig. 6 Pressure dependence of the unit-cell volume in $MnSe_2$. Squares and circles denote the experimental data obtained for the pyrite-type and arsenopyrite-type phases; solid squares denote the compression data, while open squares and solid circles denote decompression data. The solid lines represent the fitting results obtained using the second-order Birch–Murnaghan equation of state with a fixed $K' = 4$

To check the effect of hydrostaticity on the structural evolution of $MnSe_2$, a series of experiments was performed under non-hydrostatic conditions without using a pressure transmitting medium. The XRD patterns collected from experiments under non-hydrostatic conditions are depicted in Fig. 7. It can be seen that the widths of the diffraction peaks are relatively larger than those found under quasi-hydrostatic conditions (see Fig. 3a). With increasing pressure, some new diffraction peaks begin to emerge in the diffraction patterns at pressures of 13.0 GPa and above, implying that a phase transition occurs. The phase transition is completed at around 17.0 GPa. The new high-pressure phase under non-hydrostatic conditions is inferred to have the same crystal structure as that under quasi-hydrostatic conditions because the diffraction patterns are identical to each other. During the decompression process, the high-pressure phase begins to transit to the pyrite-type phase at around 7.1 GPa, and becomes a pure pyrite-type phase at 0.52 GPa. The evolution of the diffraction pattern under non-hydrostatic conditions is consistent with that under quasi-hydrostatic conditions, indicating that the condition of hydrostaticity does not significantly affect the structural evolution of $MnSe_2$.

A number of experimental studies have been carried out for MnS_2 and $MnTe_2$ to investigate their structural behavior and physical properties at high pressure (Bargeron et al.

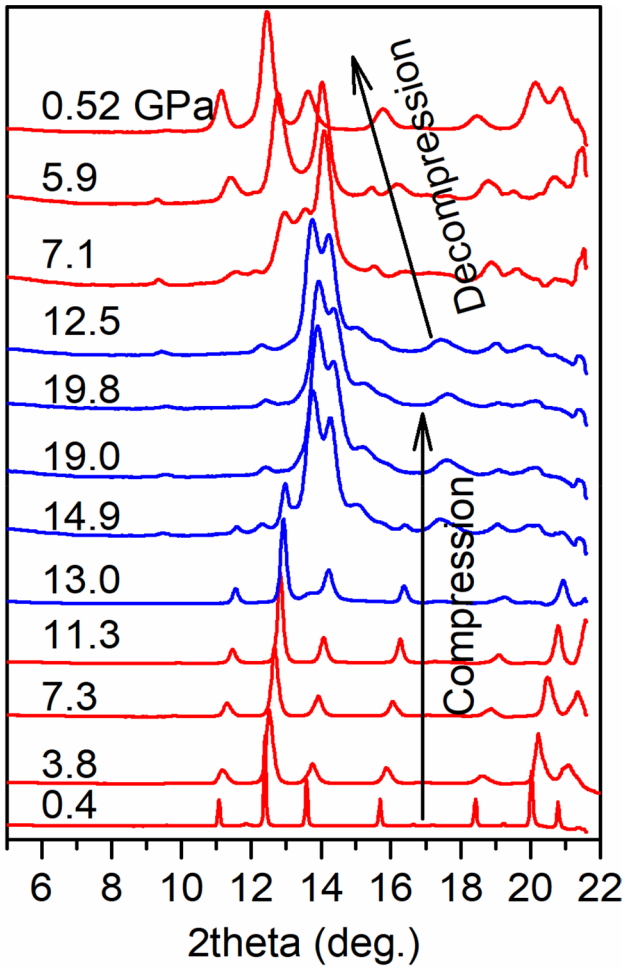

Fig. 7 The X-ray diffraction patterns collected for $MnSe_2$ during compression and decompression processes for experiments carried out under non-hydrostatic conditions without a pressure transmitting medium

1971; Chattopadhyay and Schnering 1985; Chattopadhyay et al. 1986; Durkee et al. 2019; Fjellvåg et al. 1985, 1995; Kimber et al. 2014; Vulliet et al. 2001). Even though these previous studies for MnS_2 and $MnTe_2$ observed a first-order phase transition accompanied by a large volume collapse, the derived structure for the high-pressure phase is not the same in these works. A high-pressure experimental study using conventional energy-dispersive X-ray diffraction (EDXRD) proposed that $MnTe_2$ transits from the pyrite-type structure into a marcasite structure at around 8 GPa (Fjellvåg et al. 1985), but another experimental study using synchrotron EDXRD predicted pyrite-type or/and marcasite structures for the high-pressure phase, depending on the hydrostaticity of the sample (Fjellvåg et al. 1995). Early experimental studies for MnS_2 using conventional and synchrotron EDXRD methods observed that MnS_2 transits from the pyrite-type structure into a marcasite-type structure at approximately 14 GPa (Chattopadhyay and Schnering 1985; Chattopadhyay et al. 1986). However, recent synchrotron ADXRD and XANES studies have shown that compressing pyrite-type MnS_2 to pressures above 12 GPa induces the formation of a disordered intermediate phase, which possesses a thermodynamic ground state for the arsenopyrite-type structure (Durkee et al. 2019; Kimber et al. 2014). The diffraction patterns observed for $MnSe_2$ in our present study reveal that the structural behavior of $MnSe_2$ at high pressure is almost the same as that for MnS_2. Under compression at ambient temperature, $MnSe_2$ transits from a pyrite-type structure to a disordered intermediate phase at ~ 12.5 GPa, with a thermodynamic ground state for the arsenopyrite-type structure. Both the disordered intermediate and arsenopyrite-type phases of $MnSe_2$ revert to the pyrite-type structure upon decompression to the ambient condition. In the periodic table of chemical elements, S and Se are adjacent chalcogenide elements in the VIA main group, showing similar non-metal behavior. The values of electronegativity for Se and S are 2.58 and 2.55 Pauling units respectively, very close to each other. Besides, their atom radii are also close. The close values of electronegativity and atom radius for S and Se can explain why $MnSe_2$ shows very similar high-pressure behavior to MnS_2. A recent experimental study reported that MnS and MnSe also show very similar high-pressure behavior (Wang et al. 2016).

The pyrite-type MnX_2 compounds are in a high-spin electronic state with Mn^{2+} cations containing five unpaired 3d electrons ($t_{2g}^3 e_g^2, S = \frac{5}{2}$) (Hastings et al. 1959). The high-spin MnX_2 compounds possess larger unit-cell volumes and Mn-X bond lengths compared to other pyrite-type TX_2 compounds in which transition-metal cations are in a low-spin state (Tokuda et al. 2019). Previous experimental and theoretical studies have shown that under compression, both MnS_2 and $MnTe_2$ experience a phase transition with a large unit-cell volume collapse, which is related to an electronic transition from the high-spin state ($t_{2g}^3 e_g^2, S = \frac{5}{2}$) to low-spin state ($t_{2g}^5 e_g^0, S = \frac{1}{2}$) for Mn^{2+} (Bargeron et al. 1971; Persson et al. 2006; Perucchi et al. 2009; Sidorov et al. 2011; Ueda et al. 2002). In this study, we found that $MnSe_2$ undergoes a first-order phase transition accompanied by a large volume collapse of 19%. Such a phase transition can also be a result of the HS–LS transition of Mn^{2+} in $MnSe_2$. However, further experimental studies using methods such as X-ray emission spectroscopy are required to confirm such a HS–LS transition more directly.

A structural transition for materials, especially that correlated with a spin-state electronic transition, is always accompanied by a substantial modification of the physical properties, such as elasticity, magnetism and electrical conductivity (Lin et al. 2013; Yang et al. 2015). Infrared reflection spectroscopy combined with a diamond-anvil cell

provides an effective technique to probe the electronic structures of materials, especially, the pressure-induced insulator–metal transition (Kobayashi 2001; Okamura et al. 2017). High-pressure infrared reflection spectroscopic measurements have previously confirmed that the first-order phase transition in $MnTe_2$ with a large volume reduction (~ 16%) is accompanied by an insulator to metal transition (Mita et al. 2005), agreeing well with the electrical resistance measurements for $MnTe_2$ (Vulliet et al. 2001). To explore whether or not pressure-induced metallization occurs in $MnSe_2$, we performed infrared reflection measurements for $MnSe_2$ over a wavenumber range of 600–7500 cm^{-1} at pressures up to 28.3 GPa. Pure $MnSe_2$ powder was compressed into the sample chamber without using a pressure transmitting medium so as to improve the signal-to-noise ratio. The IR reflectivity spectra collected at various pressures are depicted in Fig. 8. The spectral features observed between 1600 and 2600 cm^{-1} (marked by dashed lines) mainly arise from the strong absorbance of diamond in this wavenumber region. Because the IR reflectivity, especially at low wavenumber, is related to the carrier concentration, the IR reflectivity for $MnSe_2$ at 800 cm^{-1} is plotted as a function of pressure, as displayed in the inset in Fig. 8. It can be seen that the IR reflectivity at 800 cm^{-1} is relatively low at pressures below 12.0 GPa, but which increases suddenly upon further compression, finally becoming pressure-insensitive with a high value of ~ 0.34 at pressures above 20 GPa. The sudden increase in IR reflectivity occurs at the same pressure as the first-order phase transition from a pyrite-type structure to a disordered intermediate phase. Many transition-metal compounds such as VO_2 and MnO undergo pressure-induced metallization, as revealed by IR reflectivity measurements combined with a diamond-anvil cell (Li et al. 2017; Mita et al. 2005; Zhang et al. 2018). It is found that as the insulator–metal transition takes place, the IR reflectivity for these compounds increases abruptly, and then becomes pressure independent at a high value when the metallic state is achieved, implying that the carrier concentration does not change anymore with pressure in the metallic state. Therefore, the variation in the IR reflectivity with pressure observed for $MnSe_2$ in this study can be interpreted to reflect that $MnSe_2$ starts to transit from an insulator to metallic phase at around 13.3 GPa and that this transition is accomplished at a pressure of around 20 GPa.

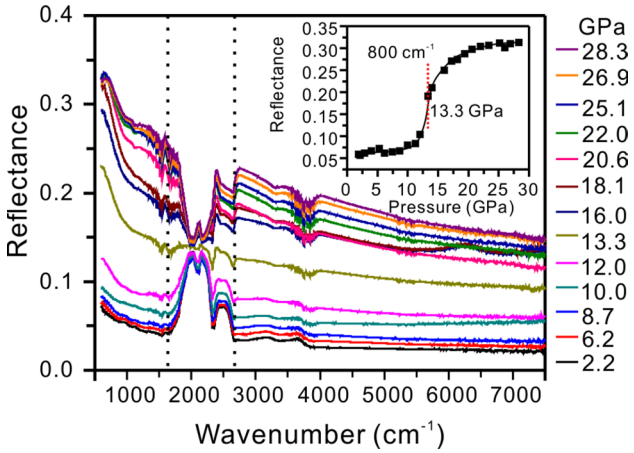

Fig. 8 Representative infrared reflectivity spectra for $MnSe_2$ upon compression. The spectral profiles measured between the two dashed lines are due to the strong absorption of diamond in the wavenumber range of 1600–2600 cm^{-1}. The inset shows the pressure dependence of the reflectivity at 800 cm^{-1}

It is intriguing that both MnS and MnSe undergo a phase transition from an insulative rocksalt-type structure (cubic, P *m* 3 *m*) to a metallic MnP-type structure (orthorhombic, P*nma*) at around 30 GPa, coupled with a giant lattice collapse (ΔV ~ 22%) and a HS–LS spin transition (Wang et al. 2016). In the metallic phase of MnS and MnSe, Mn^{2+} cations form Mn–Mn networks via metallic Mn–Mn bonds with a bond length of ~ 2.6–2.7 Å (Wang et al. 2016). In the arsenopyrite-type phase of MnS_2, even though Mn^{2+} cations form Mn–Mn dimers with a metallic bond length of ~ 2.7 Å, the Mn–Mn distance between two neighboring dimers is around 3.4 Å, which is much larger than that for Mn–Mn metallic bonds. Hence, a metallic state is not predicted to occur (Kimber et al. 2014). However, evidence from both infrared reflectivity and electrical resistance experiments have clarified that $MnTe_2$ transits into a metallic state with a pyrite-type structure at high pressure (Mita et al. 2008; Vulliet et al. 2001). Here, we explain the metallic behavior of $MnSe_2$ in the disordered intermediate phase as being a result of the closure of the *p–d* charge-transfer gap (Δ) for the centered Mn^{2+} cation and six Se^{2-} anion ligands in the $MnSe_6$ octahedrons in the disordered intermediate phase of $MnSe_2$, similar to that for the pressure-induced metallization of $MnTe_2$. It is possible that the metal-like behavior can disappear when the disordered intermediate phase of $MnSe_2$ crystalizes into the ideal arsenopyrite-type structure after laser heating.

Conclusions

In summary, we have investigated the structural and electronic properties of pyrite-type $MnSe_2$ at high pressure using synchrotron ADXRD and infrared reflection spectroscopic techniques equipped with a diamond-anvil cell. Our experimental results show that $MnSe_2$ undergoes a structural transition from a pyrite-type structure to a disordered intermediate phase with a ground state composed of an arsenopyrite-type structure, which starts at around 12.5 GPa and is completed at around 16.5 GPa upon compression. Such a phase transition is reversible and cannot be obviously

affected by hydrostatic conditions. The disordered intermediate phase is found to be in a metallic state, as indicated by its infrared reflectivity. The pyrite-arsenopyrite transition for $MnSe_2$ is coupled to a large volume collapse ($\Delta V \sim 19\%$) and a HS–LS spin transition for Mn^{2+}. The isothermal bulk modulus for the pyrite-type and arsenopyrite-type phases was determined to be $K_0 = 56.1(9)$ GPa and $K_0 = 93.1(4)$ GPa, respectively, by fitting the pressure–volume data using the second-order Birch–Murnaghan equation of state and fixing the pressure derivation of the bulk modulus at $K' = 4$. These results provide new insight to understand the structural behavior and physical properties of pyrite-type MnX_2 compounds under extreme compression.

Acknowledgements We would like to thank Prof. T. Tsuchiya for his editorial handling and valued suggestions. Constructive comments and suggestions of two anonymous reviewers greatly helped to improve the manuscript and are sincerely acknowledged. High-pressure XRD experiments were carried out at the BL15U1 beamline of Shanghai Synchrotron Radiation Facility (SSRF) and the 4W2 High Pressure Beamline of Beijing Synchrotron Radiation Facility (BSRF), respectively. This research was financially supported by the Strategic Priority Research Program (B) of the Chinese Academy of Sciences (Grant No. XDB18000000) and the National Natural Science Foundation of China (Grants No. 41874107, 41574079, 41174072). This is contribution No. IS-2903 from GIGCAS.

References

Bargeron C, Avinor M, Drickamer H (1971) Effect of pressure on the spin state of iron (II) in manganese (IV) sulfide. Inorg Chem 10:1338–1339

Bither TA, Bouchard R, Cloud W, Donohue P, Siemons W (1968) Transition metal pyrite dichalcogenides. High-pressure synthesis and correlation of properties. Inorg Chem 7:2208–2220

Chandra U, Zuburtikudis I, Parthasarathy G, Sreedhar B (2014) High-pressure electrical resistivity and Mössbauer spectroscopic studies on narrow band $Co_{0.8}Fe_{0.2}S_2$ nanoparticles up to 8 GPa. Phase Transit 87:477–490

Chattopadhyay T, Von Schnering H (1985) High pressure X-ray diffraction study on p-FeS_2, m-FeS_2 and MnS_2 to 340 kbar: a possible high spin-low spin transition in MnS_2. J Phys Chem Solids 46:113–116

Chattopadhyay T, von Schnering H, Grosshans W (1986) High pressure x-ray diffraction study on the structural phase transition in MnS_2. Physica B + C 139:305–307

Chattopadhyay T, Rossat-Mignod J, Fjellvåg H (1987) Magnetic ordering in $MnSe_2$. Solid State Commun 63:65–67

Cohen RE, Mazin I, Isaak DG (1997) Magnetic collapse in transition metal oxides at high pressure: implications for the earth. Science 275:654–657

Durkee D, Smith D, Torchio R, Petitgirard S, Briggs R, Kantor I, Evans SR, Chatterji T, Irifune T, Pascarelli S (2019) Electronic origins of the giant volume collapse in the pyrite mineral MnS_2. J Solid State Chem 269:540–546

Faber MS, Lukowski MA, Ding Q, Kaiser NS, Jin S (2014) Earth-abundant metal pyrites (FeS_2, CoS_2, NiS_2, and their alloys) for highly efficient hydrogen evolution and polysulfide reduction electrocatalysis. J Phys Chem C 118:21347–21356

Fan DW, Ma MN, Zhou WG, Wei SY, Chen ZQ, Xie HS (2011) X-ray diffraction study of arsenopyrite at high pressure. Phys Chem Miner 38:95–99

Feng ZY, Yang Y, Zhang JM (2018) The structural, electronic and magnetic properties of CoS_2 under pressure. Solid State Commun 273:60–65

Fjellvåg H, Kjekshus A, Chattopadhyay T, Hochheimer H, Hönle W, Von Schnering H (1985) Pressure induced phase transition in $MnTe_2$. Phys Lett A 112:411–413

Fjellvåg H, Grosshans W, Hönle W, Kjekshus A (1995) Pressure induced phase transition in $MnTe_2$ studied by synchrotron radiation—comparison with $RuTe_2$. J Magn Magn Mater 145:118–124

Gudelli VK, Kanchana V, Appalakondaiah S, Vaitheeswaran G, Valsakumar M (2013) Phase stability and thermoelectric properties of the mineral FeS_2: an ab initio study. J Phys Chem C 117:21120–21131

Hastings J, Elliott N, Corliss L (1959) Antiferromagnetic structures of MnS_2, $MnSe_2$, and $MnTe_2$. Phys Rev 115:13

Honig J, Spałek J (1998) Electronic properties of $NiS_{2-x}Se_x$ single crystals: from magnetic Mott−Hubbard insulators to normal metals. Chem Mater 10:2910–2929

Houari A, Blöchl PE (2018) Density functional study of half-metallicity and spin polarization in $Fe_{1-x}T_xS_2$ with T= Mn, Ni. J Phys: Condens Matter 30:305501

Huang S, Wu X, Qin S (2018) Ultrahigh-pressure phase transitions in FeS_2 and FeO_2: implications for super-earths' deep interior. J Geophys Res Solid Earth 123:277–284

Kakihana M, Matsuda TD, Higashinaka R, Aoki Y, Nakamura A, Aoki D, Harima H, Hedo M, Nakama T, Ōnuki Y (2018) Superconducting and fermi surface properties of pyrite-type compounds CuS_2 and $CuSe_2$. J Phys Soc Jpn 88:014702

Kan M, Adhikari S, Sun Q (2014) Ferromagnetism in MnX_2 (X = S, Se) monolayers. Phys Chem Chem Phys 16:4990–4994

Kimber SA, Salamat A, Evans SR, Jeschke HO, Muthukumar K, Tomić M, Salvat-Pujol F, Valentí R, Kaisheva MV, Zizak I (2014) Giant pressure-induced volume collapse in the pyrite mineral MnS_2. Proc Natl Acad Sci 111:5106–5110

Kobayashi M (2001) Infrared spectroscopy of pressure-induced metallization in semiconductors. Physica Status Solidi (b) 223:55–64

Lauer S, Trautwein A, Harris F (1984) Electronic-structure calculations, photoelectron spectra, optical spectra, and Mössbauer parameters for the pyrites MS_2 (M= Fe Co, Ni, Cu, Zn). Phys Rev B 29:6774

Li Q, Zhang H, Lin C, Tian F, Smith JS, Park C, Liu B, Shen G (2017) Pressure-induced phase transitions and insulator-metal transitions in VO_2 nanoparticles. J Alloys Compd 709:260–266

Lin JF, Speziale S, Mao Z, Marquardt H (2013) Effects of the electronic spin transitions of iron in lower mantle minerals: implications for deep mantle geophysics and geochemistry. Rev Geophys 51:244–275

Mao H, Xu JA, Bell P (1986) Calibration of the ruby pressure gauge to 800 kbar under quasi-hydrostatic conditions. J Geophys Res Solid Earth 91:4673–4676

Mita Y, Izaki D, Kobayashi M, Endo S (2005) Pressure-induced metallization of MnO. Phys Rev B 71:100101

Mita Y, Ishida Y, Kobayashi M, Endo S (2008) Infrared reflection of $MnTe_2$ under high pressure. Acta Physica Pol Ser A Gen Phys 113:617–620

Nishio-Hamane D, Yagi T (2009) Equations of state for postperovskite phases in the $MgSiO_3$–$FeSiO_3$–$FeAlO_3$ system. Phys Earth Planet Inter 175:145–150

Ogawa S (1979) Magnetic properties of 3d transition-metal dichalcogenides with the pyrite structure. J Appl Phys 50:2308–2311

Okamura H, Ikemoto Y, Moriwaki T, Nanba T (2017) Infrared spectroscopy techniques for studying the electronic structures of materials under high pressure. Jpn J Appl Phys 56:05FA11

Pathak M, Tamang D, Kandasamy M, Chakraborty B, Sekhar Rout C (2020) A comparative experimental and theoretical investigation on energy storage performance of $CoSe_2$, $NiSe_2$ and $MnSe_2$ nanostructures. Appl Mater Today 19:100568

Persson K, Ceder G, Morgan D (2006) Spin transitions in the $Fe_xMn_{1-x}S_2$ system. Phys Rev B 73:115201

Perucchi A, Marini C, Valentini M, Postorino P, Sopracase R, Dore P, Hansmann P, Jepsen O, Sangiovanni G, Toschi A (2009) Pressure and alloying effects on the metal to insulator transition in $NiS_{2-x}Se_x$ studied by infrared spectroscopy. Phys Rev B 80:073101

Prescher C, Prakapenka VB (2015) DIOPTAS: a program for reduction of two-dimensional X-ray diffraction data and data exploration. HPR 35:223–230

Rabia K, Baldassarre L, Deisenhofer J, Tsurkan V, Kuntscher CA (2014) Evolution of the optical properties of chromium spinels $CdCr_2O_4$, $HgCr_2S_4$, and $ZnCr_2Se_4$ under high pressure. Phys Rev B 89:125107

Reich M, Deditius A, Chryssoulis S, Li JW, Ma CQ, Parada MA, Barra F, Mittermayr F (2013) Pyrite as a record of hydrothermal fluid evolution in a porphyry copper system: a SIMS/EMPA trace element study. Geochim Cosmochim Acta 104:42–62

Sidorov V, Krasnorussky V, Petrova AE, Utyuzh A, Yuhasz W, Lograsso TA, Thompson J, Stishov SM (2011) High-pressure study of the phase transition in the itinerant ferromagnet CoS_2. Phys Rev B 83:060412

Sidorov VA, Guo J, Sun L, Brazhkin VV (2018) Thermodynamics of a magnetic transition in MnS_2 at high pressures. JETP Lett 107:311–314

Temmerman W, Durham P, Vaughan D (1993) The electronic structures of the pyrite-type disulphides (MS2, where M= Mn, Fe Co, Ni, Cu, Zn) and the bulk properties of pyrite from local density approximation (LDA) band structure calculations. Phys Chem Miner 20:248–254

Toby BH (2001) EXPGUI, a graphical user interface for GSAS. J Appl Crystallogr 34:210–213

Tokuda M, Yoshiasa A, Mashimo T, Arima H, Hongu H, Tobase T, Nakatsuka A, Sugiyama K (2019) Crystal structure refinement of $MnTe_2$, $MnSe_2$, and MnS_2: cation–anion and anion–anion bonding distances in pyrite-type structures. Zeitschrift für Kristallographie-Cryst Mater 234:371–377

Tossell J, Vaughan D, Burdett J (1981) Pyrite, marcasite, and arsenopyrite type minerals: crystal chemical and structural principles. Phys Chem Miner 7:177–184

Ueda H, Nohara M, Kitazawa K, Takagi H, Fujimori A, Mizokawa T, Yagi T (2002) Copper pyrites CuS_2 and $CuSe_2$ as anion conductors. Phys Rev B 65:155104

Vulliet P, Sanchez J, Braithwaite D, Amanowicz M, Malaman B (2001) Pressure-induced metallization and collapse of the antiferromagnetic state of $MnTe_2$. Phys Rev B 63:184403

Wang L, Chen L, Luo T, Bao K, Qian Y (2006) A facile method to the cube-like $MnSe_2$ microcrystallines via a hydrothermal process. Solid State Commun 138:72–75

Wang Y, Bai L, Wen T, Yang L, Gou H, Xiao Y, Chow P, Pravica M, Yang W, Zhao Y (2016) Giant pressure-driven lattice collapse coupled with intermetallic bonding and spin-state transition in manganese chalcogenides. Angew Chem Int Ed 55:10350–10353

Wu MH, Chou WJ, Huang JS, Putungan DB, Lin SH (2019) First-principles investigation of the hydrogen evolution reaction on different surfaces of pyrites MnS_2, FeS_2, CoS_2, NiS_2. PCCP 21:21561–21567

Yang J, Tong X, Lin JF, Okuchi T, Tomioka N (2015) Elasticity of ferropericlase across the spin crossover in the Earth's lower mantle. Sci Rep 5:1–9

Yonggang GY, Ross NL (2010) Prediction of high-pressure polymorphism in NiS_2 at megabar pressures. J Phys Condens Matter 22:235401

Yu L, Yang JF, Lou XW (2016) Formation of CoS_2 nanobubble hollow prisms for highly reversible lithium storage. Angew Chem Int Ed 55:13422–13426

Zhang H, Li Q, Wang F, Liu R, Mao Y, Liu Z, Li X, Yang K, Cui T, Liu B (2018) Pressure-induced reversible phase transitions in a new metastable phase of vanadium dioxide. J Phys Chem C 123:955–962